

2D multiresolution automated system for detecting BSRs on seismic reflection images

Perla Karina Barba-Rojo¹, Selene Solorza-Calderón¹ ,
Antonio González-Fernández²  and Mario González-Escobar² 

¹Facultad de Ciencias, Universidad Autónoma de Baja California, Km.103 Carretera Tijuana-Ensenada, C. P. 22860, Ensenada B.C., Mexico

²División de Ciencias de la Tierra, CICESE, Carretera Ensenada-Tijuana No. 3918, Zona Playitas, C.P. 22860, Ensenada B.C., Mexico

E-mail: selene.solorza@uabc.edu.mx

Received 15 February 2018, revised 8 May 2018

Accepted for publication 6 June 2018

Published 20 July 2018



CrossMark

Abstract

This work presents an automation system for detecting the presence of bottom-simulating reflectors (BSRs) and other reflectors parallel to the sea bottom in real seismograms. The system uses automatic gain control to aid the thresholding method for edge detection and segmentation to calculate the sea bottom curve. After preprocessing the seismic reflection images, 2D multiresolution analysis methodology was used to develop the automated pattern recognition system which detects BSRs and other parallel reflectors in a robust manner. Synthetic and real seismic images were used to evaluate the proposed methodology, which showed excellent results in both cases.

Keywords: BSR, MRA, wavelet transform, pattern recognition algorithms, seismic attributes

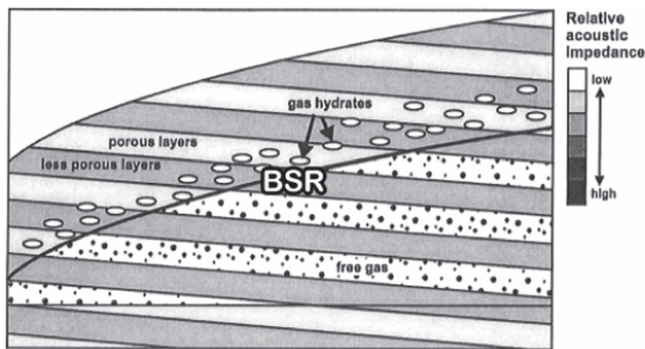
(Some figures may appear in colour only in the online journal)

1. Introduction

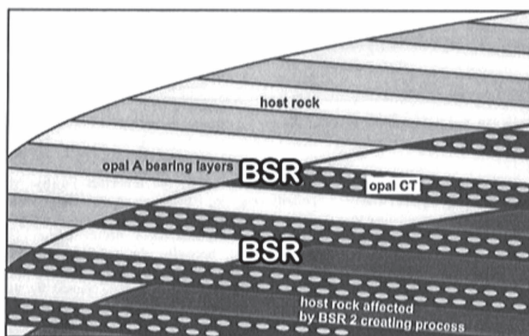
A bottom-simulating reflector or BSR is commonly used as a geophysical interpretation marker for the presence of gas hydrates (Rodrigo *et al* 2009, 2009). A BSR is formed by processes that depend on the sub-bottom depth and the contrast of velocities between layers, in turn influencing the pressure and temperature in the sediment (MacKay *et al* 1994, Holbrook *et al* 1996, Pecher *et al* 1996, Bünz and Mienert 2004). The study of the role played by gas hydrates and free gas in ocean temperature, sea level, and climate changes is an active field of research (Majorowicz and Osadetz 2003, Oellrich 2004, Koh and Sloan 2007, Boswell and Collett 2011, Klitzke *et al* 2016, Aregbe 2017, Ruppel and Kessler 2017, Taladay *et al* 2017, Vadakkepuliambatta *et al* 2017). The Intergovernmental Panel on Climate Change reports that greenhouse emissions are higher than ever due to atmospheric concentrations of carbon dioxide, methane and nitrous oxide (IPCC 2014). Therefore, it is crucial to estimate the methane concentrations in hydrate/free gas systems. Theoretical methods based on poroelastic Biot theory have been developed to predict the gas hydrate concentrations in

marine sediment. To determine the gas hydrate concentrations in the BSR zone, these methods use the P and S velocity fields (Carcione and Tinivella 2000, Tinivella 1999, Tinivella and Carcione 2001, Rodrigo *et al* 2009, 2009, Vargas-Cordero *et al* 2017). Hence a BSR needs to be located first.

Usually, BSR detection is performed by manual operation by a trained interpreter using the idea that a BSR generally imitates the sea bottom curve, it cuts across lithologic reflectors, and it appears as the strongest reflector in seismic records (Dobrin and Savit 1988, Tinivella 1999, Coren *et al* 2001, Nouzè *et al* 2009, Rodrigo *et al* 2009, Plaza-Faverola *et al* 2017). Because of the use of BSRs as markers of the presence of gas hydrates, it is useful for seismic interpreters to have an automated pattern recognition system to detect BSRs. Pattern recognition systems that use artificial and convolutional neural networks are specialized to identify the first-break (FB) picking of P and S waves (McCormack *et al* 1993, Sandham and Leggett 2003, Gentili and Michelini 2006, Maity *et al* 2014, Castellazzi *et al* 2015, Akram and Eaton 2016, Yuan *et al* 2018). These pattern recognition systems identify two categories, FB and non-FB. The neural networks are trained using information on the trace's



(a)



(b)

Figure 1. Types of BSRs. Reprinted from Berndt *et al* (2004), copyright 2004, with permission from Elsevier. (a) Gas-hydrate-related BSR. (b) Diagenesis-related BSR.

amplitude, phase, mean power, envelope slope of the selected peak, adjacent peaks and lateral continuity. The neural networks are also trained with the manually picked FB provided by the expert and a window centered in the region of the expected FB event of the rasterized seismic traces (using 7 to 11 adjacent traces). The goal of these neural networks is to perform pattern recognition as the trained interpreter does. Therefore, these neural networks are highly dependent on the quality of the input parameters and the corresponding labeled classification outputs. Also, convolutional neural networks (Yuan *et al* 2018) can be interactively evaluated and adjusted via three established rules. None of these neural network methodologies can be straightforwardly adapted to identify BSR curves because to detect a BSR other features are required; like a BSR it is a non-FB that mimics the sea bottom reflector (SBR). The automated system of the present proposal does not need to be trained (in contrast to neural networks) because the SBR curve's form is extracted and it is searched for in the seismic image as an expert does. This allows us to develop a more flexible system to solve a large number of cases because by not having to train the system we are not delimiting ourselves to a finite set of scenarios. Nevertheless, for cases in which the sedimentation is parallel to the SBR, the automated system will fail because in this kind of situation not even an expert can do it.

Berndt *et al* (2004) classify BSR formation into two main types. One is caused by the presence of gas hydrates (a schematic illustration of this process is shown in figure 1(a)).

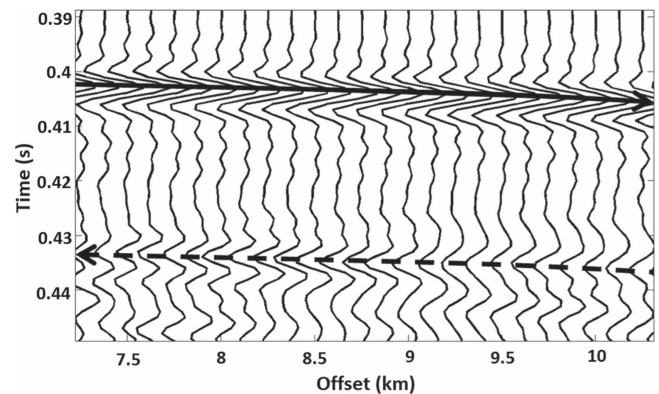


Figure 2. BSR polarity. The seismic record presents a BSR related to gas hydrates (dashed). It shows a negative polarity with respect to the SBR (continuous). The data were collected in September 2006 in Farallon Basin at the Gulf of California.

The other is related to the diagenesis stages of opal-A (amorphous) to opal-C (crystalline) to quartz—this is shown in figure 1(b). Considering that BSRs related to gas hydrates are caused by the negative acoustic impedance contrast between sediments containing gas hydrate and free gas underneath the gas hydrate stability zone, this type of BSR is characterized by negative polarity with respect to an SBR (Pecher *et al* 1996). An example of a seismic register taken from Farallon Basin in the Gulf of California with a BSR formed by gas hydrates is given in figure 2: the continuous curve marks the SBR and the dashed curve marks the BSR, which has a negative polarity with respect to the sea bottom curve.

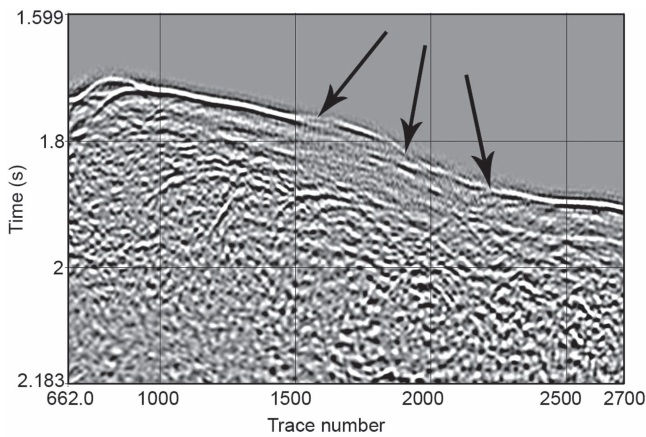
2. Method

In the proposed method, tasks such as application of seismic attributes for image enhancement, edge detection, multi-resolution analysis (MRA) and pattern recognition are performed. The pattern recognition methodology to detect BSRs is described below.

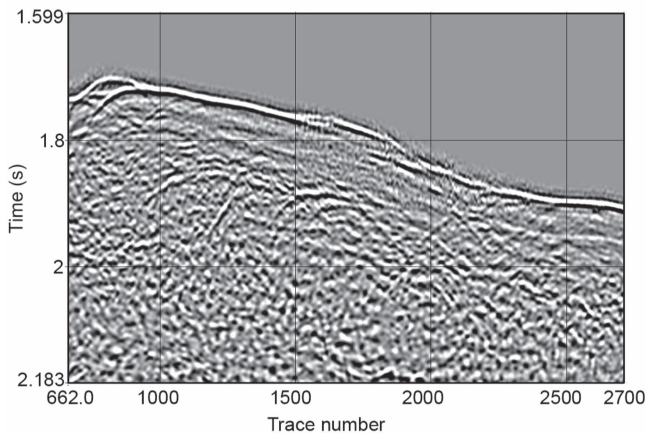
2.1. Preprocessing the seismic reflection image

2.1.1. Automatic gain control. In seismic reflection images, lateral discontinuities sometimes occur due to low amplitudes, the resolution of the data, noise, etc. One way to minimize such discontinuities is by applying an equalization process like automatic gain control (AGC). This process utilizes a gain value to each data sample; this is the amplitude average of the time window used. AGC provides vertical amplitude balance to enhance low-amplitude areas or to address more general time-variant amplitude changes. Therefore, this process applies a variable scale to each trace such that the amplitude along the entire trace is roughly uniform. Then, by minimizing amplitude variations along the trace, well-correlated but low-amplitude phases become more visible.

For example, in figure 3(a) a seismic reflection image with a lateral variation of the amplitudes of an SBR is



(a)



(b)

Figure 3. Improvement of sea bottom signal using AGC. (a) Apparent lateral discontinuities of SBR. (b) AGC applied to data using a window of 200 ms.

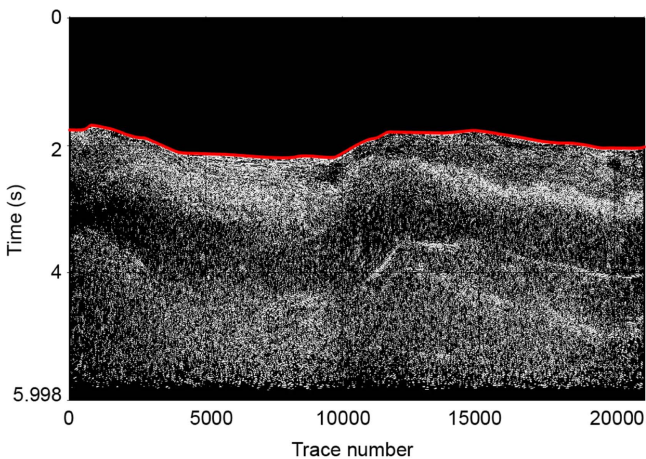
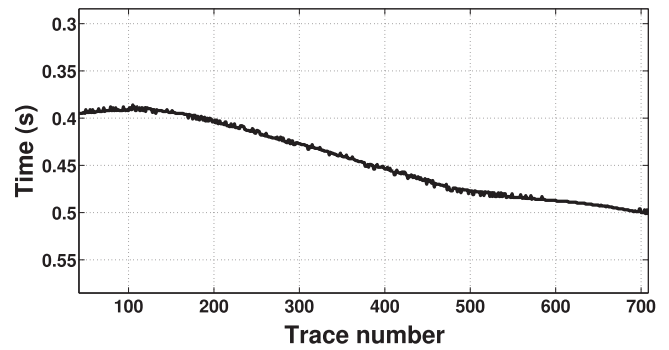
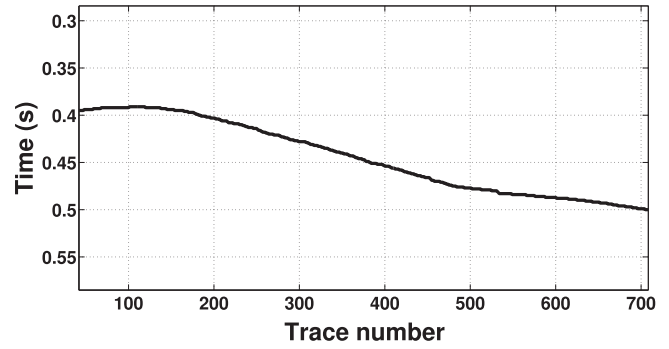


Figure 4. Threshold image and detected sea bottom line.

presented. When applying AGC using a window of 200 ms in figure 3(a), it is possible to reduce such variation, as shown in figure 3(b). By applying such a short window, the sea bottom should be the strongest reflector, thus ensuring that the next step can be performed reliably.



(a)



(b)

Figure 5. Median filter applied to the SBR. (a) Detected SBR through threshold image. (b) Median-filtered SBR.

2.2. SBR detection and segmentation

Once we have ensured that the sea bottom amplitude is maximized, the next step is to obtain the sea bottom shape. Detection of the sea bottom is performed by applying a thresholding method to the AGC-preprocessed seismic reflection image.

2.2.1. Thresholding. In this work, an automated method is used to select the threshold value given by Gonzalez and Woods (2008). This procedure allows us to eliminate lower amplitudes and reflections above the sea bottom and preserve higher amplitudes.

The methodology is performed as follows:

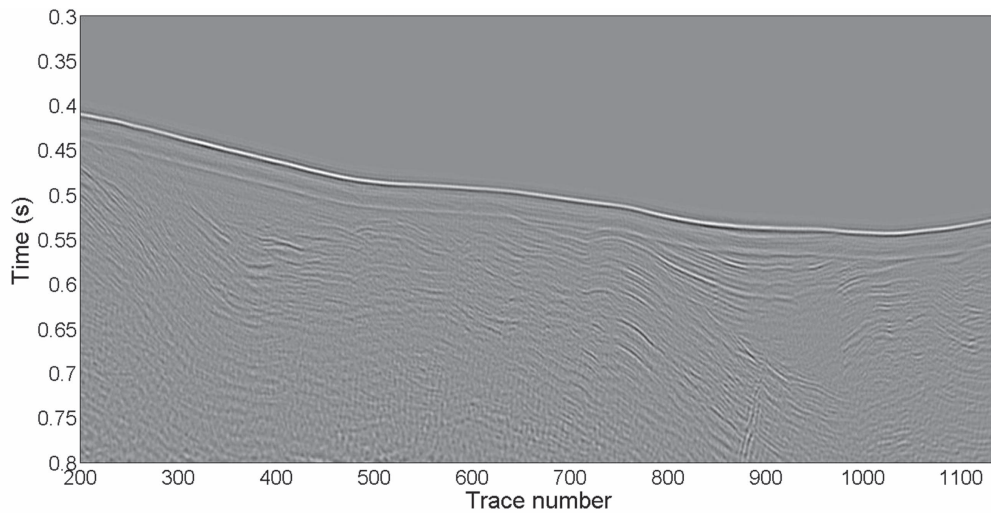
- (i) An initial threshold value τ_0 is selected as the midpoint between the minimum and maximum intensity values in the image, that is

$$\tau_0 = \frac{\max(I(x, y)) + \min(I(x, y))}{2}, \quad (1)$$

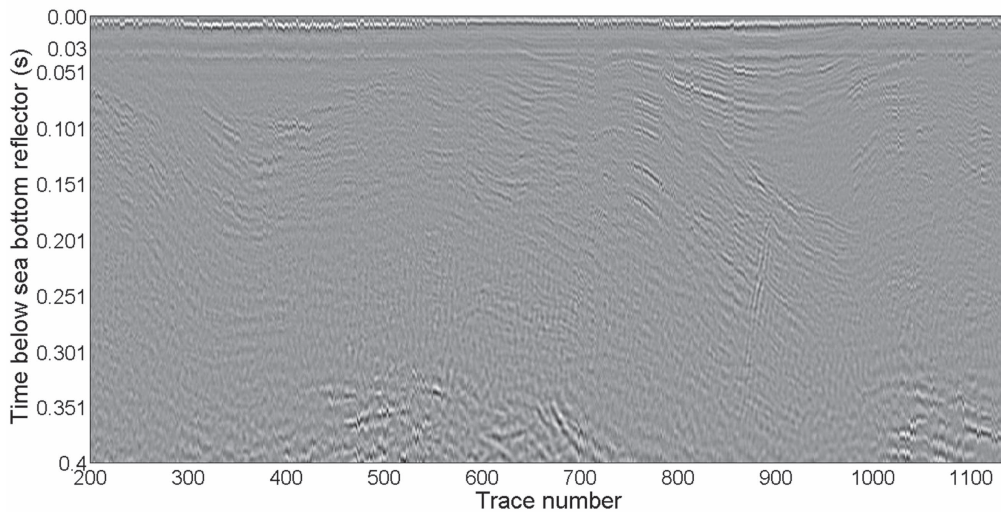
where $x = 1, \dots, M$ and $y = 1, \dots, N$. Here, it considers the intensity value range of the image.

- (ii) Build the following two sets,

$$A_1 = \{(x, y): I(x, y) \leq \tau_{n-1}, x = 1, \dots, M, y = 1, \dots, N\}, \quad (2)$$



(a)



(b)

Figure 6. Straightened sea bottom line. (a) Original seismogram. (b) Straightened seismogram.

$$A_2 = \{(x, y): I(x, y) > \tau_{n-1}, x = 1, \dots, M, y = 1, \dots, N\}, \tag{3}$$

where $n = 1, 2, \dots$ represents the iteration step. In this part, the intensity value range is divided into two sets.

(iii) Obtain μ_1 from A_1 and μ_2 from A_2 :

$$\mu_k = \frac{\max(I(x, y)) + \min(I(x, y))}{2}, \tag{4}$$

where $(x, y) \in A_k, k = 1, 2$. μ_k is the midpoint of the intensity values in each subrange. The image intensity value range is divided into two subranges. Therefore the intensity value range in each subrange is smaller than the intensity value range of the image.

(iv) Recalculate the threshold value:

$$\tau_n = \frac{\mu_2 + \mu_1}{2}. \tag{5}$$

(v) Repeat steps (ii) to (iv) until

$$|\tau_n - \tau_{n-1}| \leq TOL, \tag{6}$$

that is, the difference between the threshold value obtained in the n -iteration (τ_n) and the threshold value of the $(n - 1)$ -iteration (τ_{n-1}) is smaller than the desired tolerance TOL . In this work, $TOL = 1 \times 10^{-1}$.

Figure 4 shows the binary image resulting from an image processing applying a threshold value of 97 (intensity value) on the AGC-preprocessed seismic reflection image.

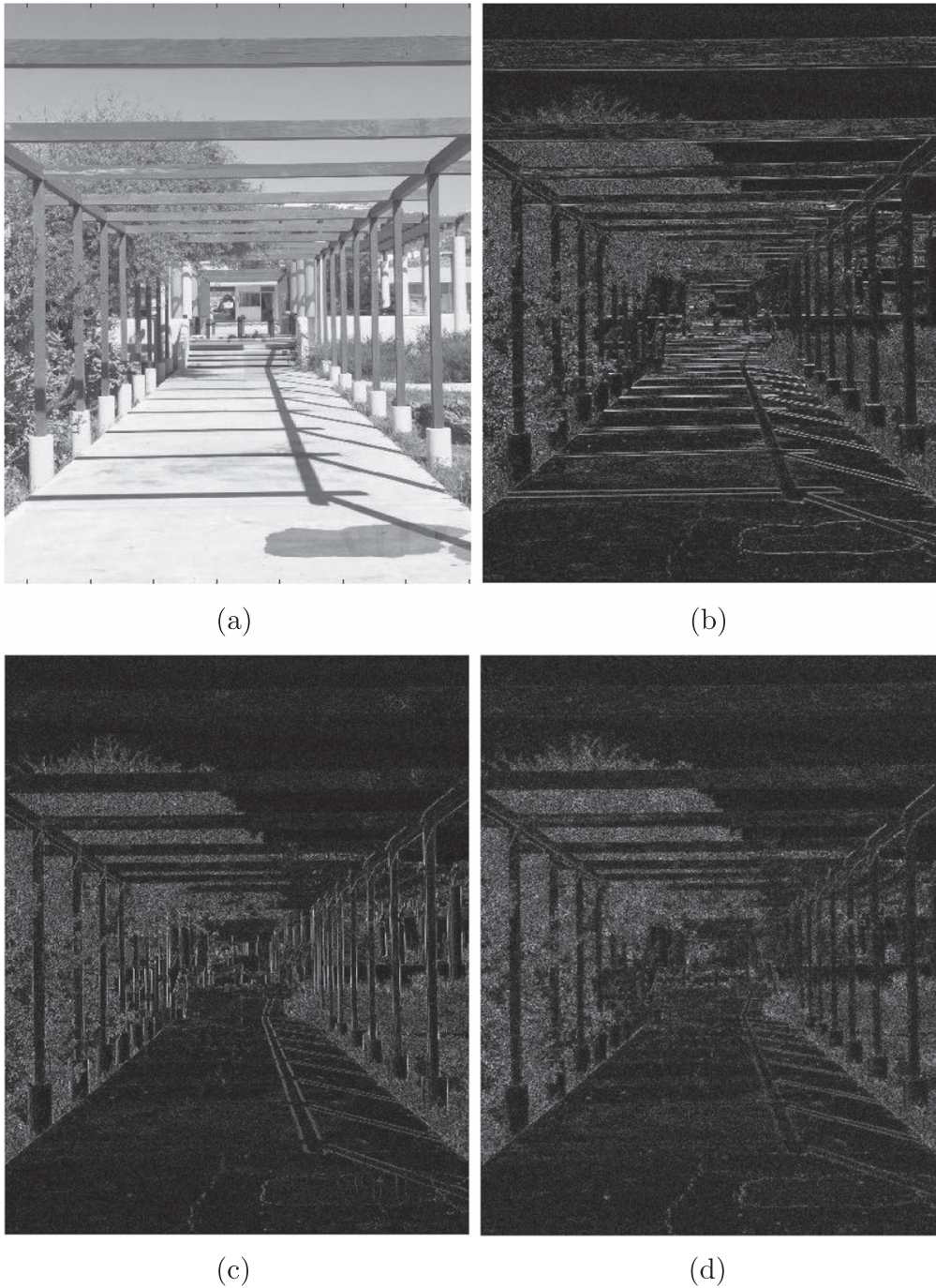


Figure 7. 2D MRA decomposition example. (a) LL sub-signal. (b) HL sub-signal. (c) LH sub-signal. (d) HH sub-signal. Photograph courtesy of L. J. Villegas-Vicencio.

2.2.2. Sea bottom extraction. Once reflections above the sea bottom are eliminated, the first non-zero amplitude value in each seismic trace $\tilde{x}_i(t)$ corresponds to the SBR. Therefore this yields a straightforward manner of extracting the sea bottom curve by

$$SBR = \{(t_0^{(i)}, \tilde{x}_i(t_0^{(i)})) | i = 1, \dots, N; t_0^{(i)} \in [0, t_n] \text{ is the smallest real value for which } \hat{x}_i(t_0^{(i)}) \neq 0\}, \quad (7)$$

where t_n is the last recorded time of the seismogram, $\hat{x}_i(t)$ is the trace in the threshold image corresponding to the

trace $\tilde{x}_i(t)$, and N is the number of traces in the seismic image.

In order to get a smoother curve, a median filter was applied to it. The median filter replaces each value with the median of the values in the selected window (in this work the length of the window is 10 pixels for synthetic seismograms and 50 pixels for real seismograms). The curve is displayed in figure 5, the filtered SBR in figure 5(b) and the one extracted initially from the threshold image in figure 5(a).

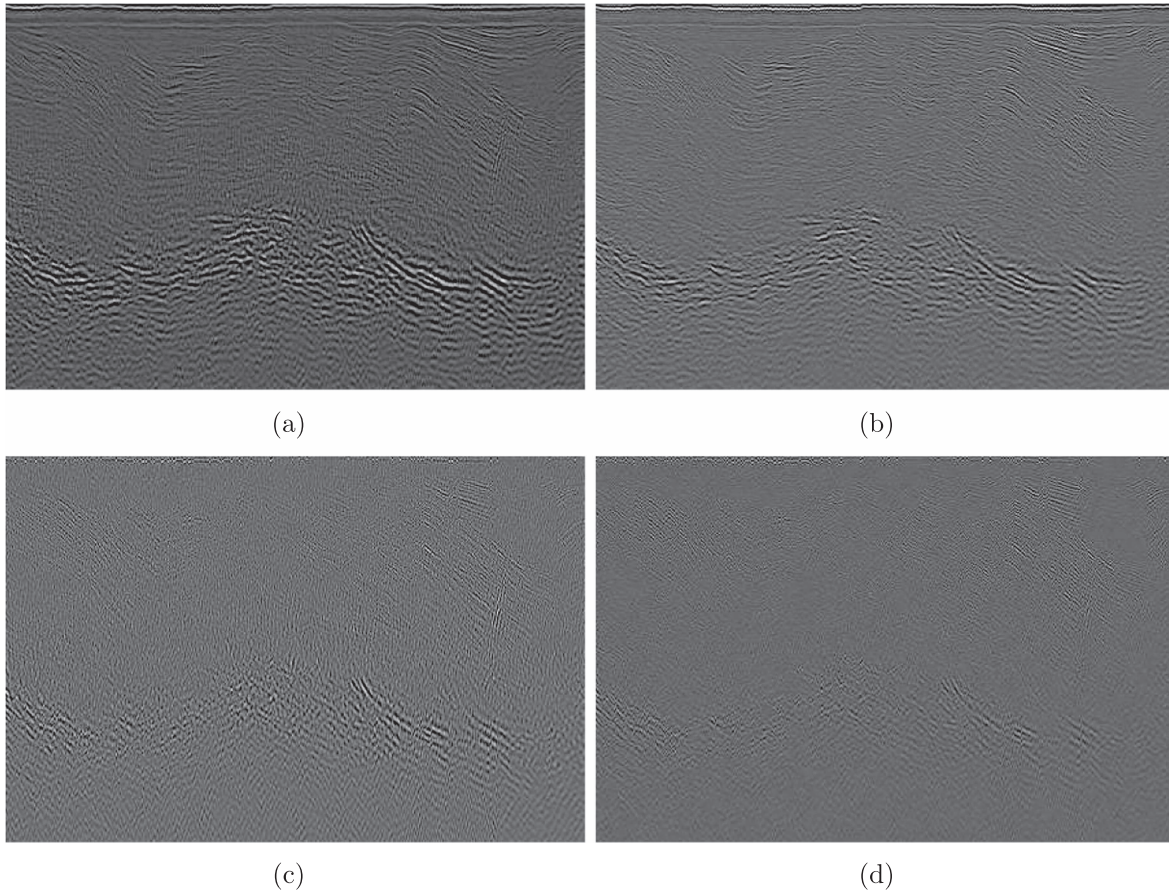


Figure 8. MRA decomposition applied to figure 6(b). (a) LL sub-signal. (b) HL sub-signal. (c) LH sub-signal. (d) HH sub-signal.

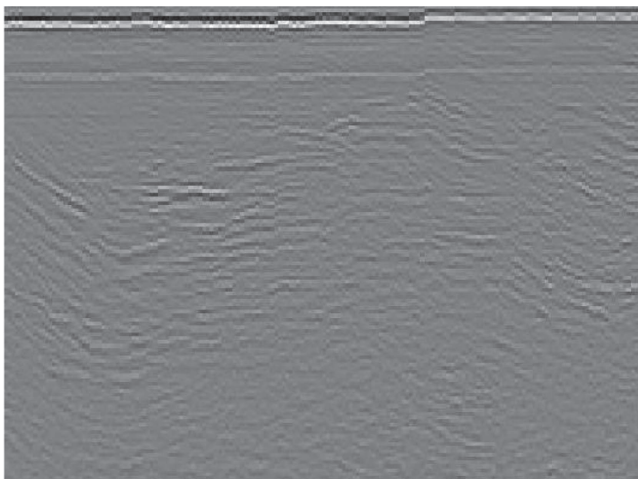


Figure 9. Amplification of the HL sub-signal in figure 8(b) around the SBR and BSR.

2.3. Detection of BSR and other parallel reflectors

The automated pattern recognition system for detecting BSRs and other parallel reflectors consists in utilizing the digitalized sea bottom curve, obtained in section 2.2.2, as the pattern to

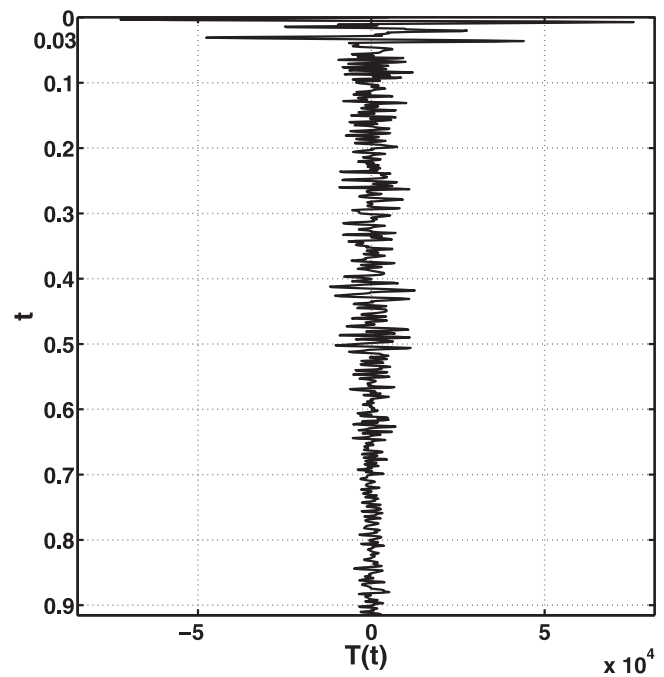


Figure 10. Sum of intensity values for each row in the HL sub-signal image.

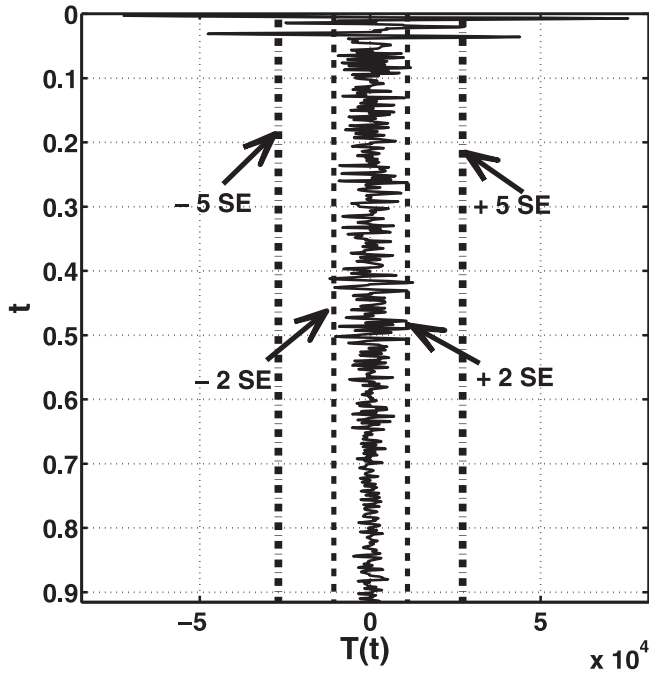


Figure 11. Discrimination criterion to identify reflectors parallel to the sea bottom.

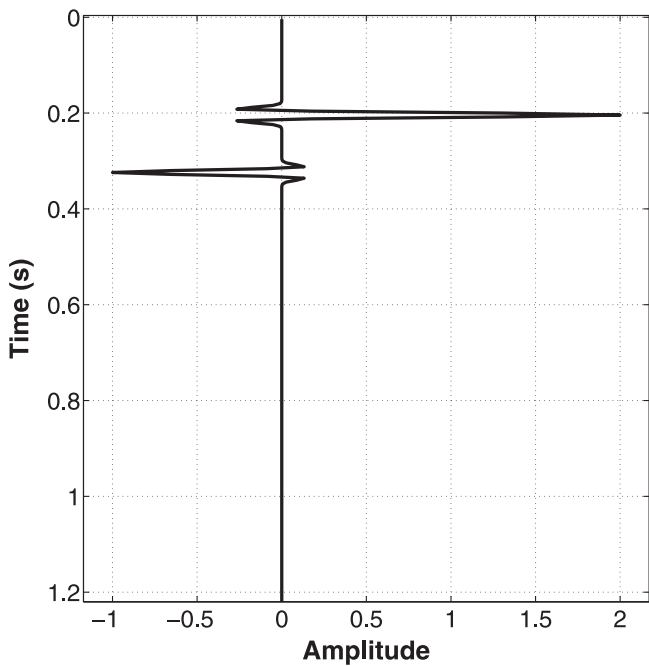


Figure 12. Synthetic trace generated with a Ricker wavelet.

be recognized. The methodology consists in straightening the sea bottom curve (consequently the BSR and other parallel reflectors will also be straightened) to apply the technique for detecting horizontal lines developed by Tang *et al* (1997), which uses 2D MRA. The first-arrivals sequence generated from the SBR detection step $\{t_0^{(i)}\}_{i=1}^N$ is used to shift up $t_0^{(i)}$ units of the trace $\tilde{x}_i(t)$. This procedure will straighten the sea bottom and all its parallel reflectors (including the BSR)—see for example figure 6(b). Tang *et al* (1997) proposed a methodology to detect horizontal lines by using the HL

sub-signals; the theoretical foundations are explicitly described in appendices A and B. The method takes advantage of the ‘enhancing’ effect on horizontal lines and the ‘smoothing’ effect on vertical lines, as shown in figure 7.

A 2D MRA decomposition applied to the straightened seismogram in figure 6(b) is displayed in figure 8, which shows that in the HL sub-signal in figure 8(b) horizontal lines are intensified, and vertical lines are diminished. In contrast to this, in the LH sub-signal in figure 8(c) horizontal lines are reduced and vertical lines are enhanced. The HH sub-signal in figure 8(d) exhibits that both horizontal and vertical lines are diminished, because only high frequencies in the two directions, such as any diagonal lines, are preserved. The LL sub-signal in figure 8(a) has all low frequencies, producing a lower-resolution version of the original straightened seismogram. For the sake of clarity, an amplification of the HL sub-signal in figure 8(b), around the SBR and BSR areas, is shown in figure 9, where both reflectors are well defined, and other non-parallel reflectors are smoothed.

The 2D MRA decomposition generates sub-signal images half the size of the original seismic image (this is due to the down-sampling scale factor of 2 in figure A1). It uses the standard image processing procedure with a scale factor of 2 and bicubic interpolation to resize the HL sub-signal (Gonzalez and Woods 2008). Once the scale is recovered, the highest intensity values are located in the sea bottom line and its parallel reflectors, as shown in figure 9. Therefore, when the intensity values of the rows in the HL image are added, the maximum values will be located at the sea bottom and BSR lines; mathematically this is given by

$$T(x) = \sum_{y=1}^N HL(x, y), \quad (8)$$

where $x = 1, \dots, M$. Because the seismic reflection image is given in time units, equation (8) is rewritten in terms of

$$t = (x - 1)f_s, \quad (9)$$

where f_s is the sampling frequency. In this work $f_s = 1000$ Hz. Figure 10 shows the graph $T(t)$ for the HL image in figure 9. As expected, the highest amplitude of the function is given in the sea bottom location. According to equation (9) it is in $t = 0$ s. The next highest peak is in the BSR location, appearing at $t = 0.03$ s below the SBR. Therefore, the function $T(t)$ provides the presence and the separation time of parallel reflectors with respect to the sea bottom; the non-parallel reflectors’ contribution is attenuated. The time series in figure 10 has a mean $\mu = 0$ and the amplitudes of the peaks corresponding to the non-parallel reflectors are confined in the interval range $[\mu - 2SE, \mu + 2SE]$ (SE represents the standard error). According to parametric statistical theory, a data set has normal distribution with mean μ and standard deviation of the form $\frac{\sigma_\mu}{\sqrt{n}} = SE$ (n is the sample size and σ_μ is the standard deviation if the data have normal distribution) (Deep 2006, Triola 2010). The range $[\mu - 2SE, \mu + 2SE]$ implies that 95.4% of the amplitude peaks of the non-parallel reflectors are confined in that region. In general, that is the case, but there are some atypical cases in which the non-parallel reflectors have amplitudes that are not confined in the region $[\mu - 2SE, \mu + 2SE]$

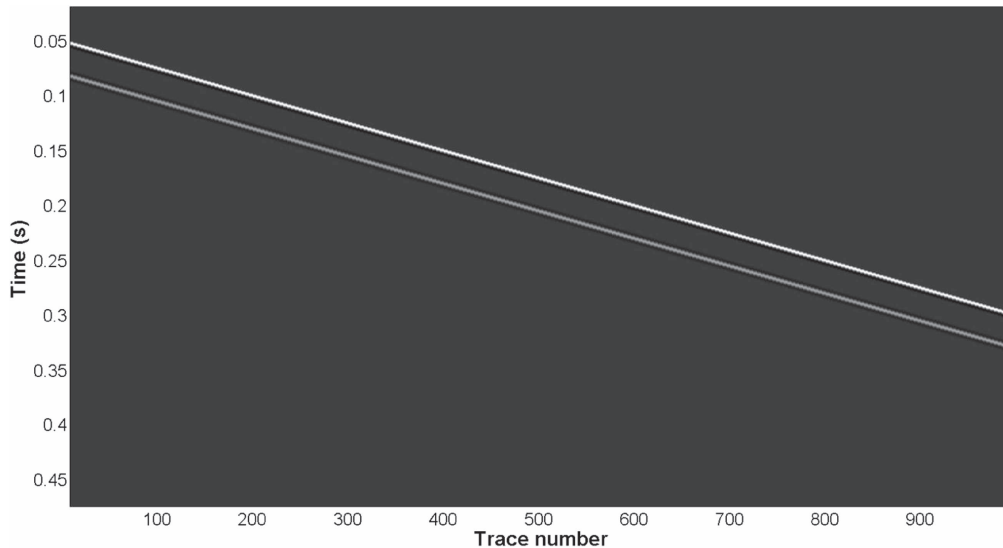


Figure 13. Diagonal SBR with opal-based BSR.

and they should be taken into account also. The experiments showed that the proper criterion to discriminate between parallel and non-parallel reflectors is $[\mu - 5SE, \mu + 5SE]$, as shown in figure 11.

3. Results

3.1. Application to synthetic seismic images

A database of synthetic seismic images was created to analyze the effectiveness of the proposed BSR automated pattern recognition methodology. A Ricker wavelet of a central frequency of 140 Hz (also known as a Mexican-hat wavelet) was used to build the images with a distance between traces of 1 m; a sample trace can be seen in figure 12. The synthetic seismic images simulate horizontal, diagonal and sinusoidal SBRs; to each of these images was added one of five different types of conditions—without a parallel reflector, an opal-based BSR, a gas-based BSR, multiple parallel facies and a deep parallel reflector—generating a total of 15 different synthetic seismic images. Figure 13 shows an example of a diagonal SBR with an opal-based BSR, and the corresponding graph of $T(t)$ in figure 14(a) indicates that the BSR appears at $t = 0.03$ s below the SBR. The automated pattern recognition system shows in black-dotted lines the SBR and BSR, as shown in figure 14(b). The proposed methodology properly locates all parallel reflectors in the 15 synthetic seismic images.

Other non-parallel reflectors and two types of discontinuities (geological faults) were added to simulate the conditions presented in real seismic reflection images. The first kind is a lateral discontinuity in each layer; these are named type-one discontinuities; in the second kind the inner layers have lateral discontinuities, and only the sea bottom layer is continuous; these are called type-two discontinuities. Figure 15 shows a sample seismic image with a sinusoidal SBR, a gas-based BSR, sinusoidal reflectors non-parallel to

the sea bottom and type-two discontinuities (geological faults). The graph of $T(t)$ in figure 16(a) indicates that the BSR appears at $t = 0.03$ s below the SBR. The automated pattern recognition system shows in black-dotted curves the SBR and BSR, as shown in the seismic image in figure 16(b). The pattern recognition system detected all parallel reflectors when other non-parallel reflectors and discontinuities (geological faults) were added. Moreover, the effectiveness of the system was tested using images with white Gaussian noise (WGN) and salt-and-pepper noise. Four scenarios were created: sea bottom and parallel reflectors; sea bottom, parallel and non-parallel reflectors; sea bottom, parallel reflectors, non-parallel reflectors and type-one discontinuities; sea bottom, parallel reflectors, non-parallel reflectors and type-two discontinuities. Each scenario is a group of 15 possible combinations of the sea bottom and parallel reflectors. For example, figure 17 shows a seismic image with a sinusoidal SBR, a gas-based BSR, sinusoidal reflectors non-parallel to the sea bottom, type-two discontinuities and WGN with a signal-to-noise ratio (SNR) of 6 dB. The corresponding graph of $T(t)$ in figure 18(a) indicates that the BSR appears at $t = 0.03$ s below the SBR and figure 18(b) shows in black-dotted curves the SBR and BSR in the seismic image. Table 1 shows the effectiveness of the pattern recognition system when the synthetic seismic images have WGN; the first column displays the SNR values in decibels, the second column shows the corresponding SNR values in percentage, and the third column gives the respective variance values. The WGN added to the image has SNR values of 10 dB, 8 dB, 6 dB, 5 dB, 3 dB, 2 dB, 1 dB and 0 dB. The system efficiency response to these study cases is indicated in columns 4 to 8. The percentages shown in table 1 were calculated using the 15 synthetic seismic images per scenario. Analogously, table 2 shows the system response when salt-and-pepper noise was added; the density value goes from 0.1 to 0.9, with a step size of 0.2.

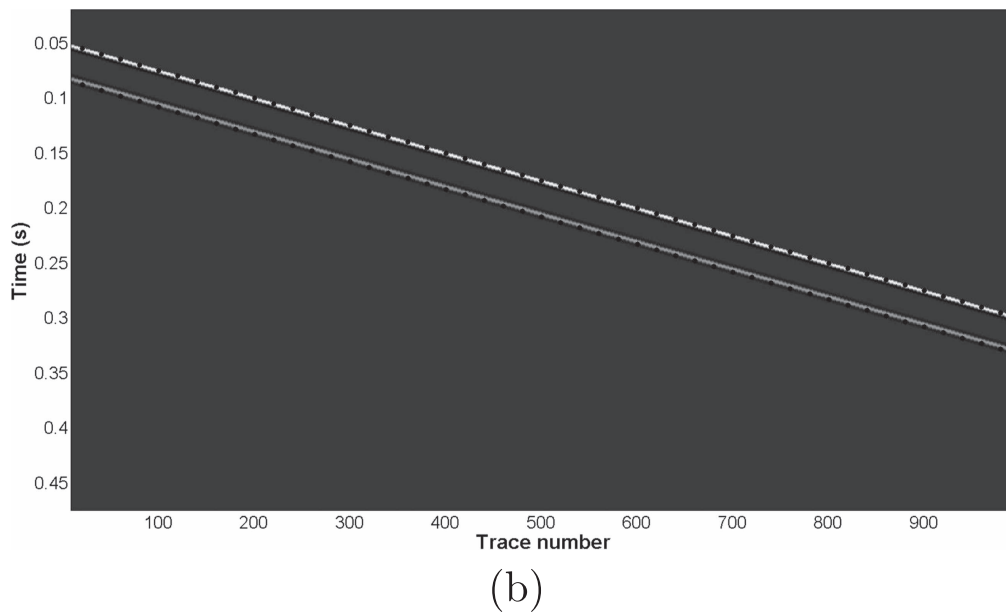
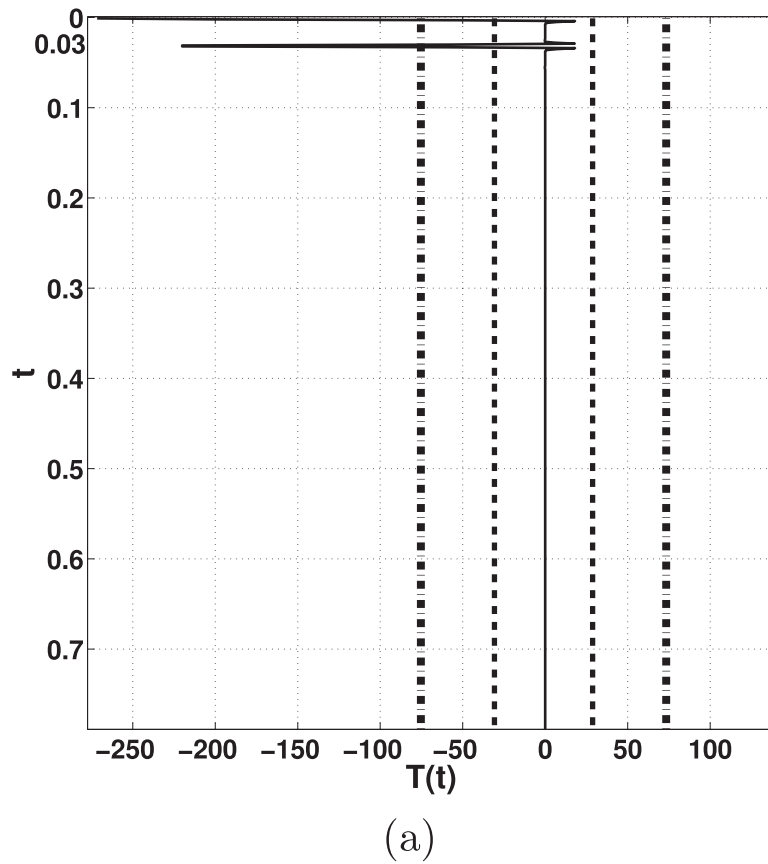


Figure 14. The pattern recognition system response for the synthetic seismic image with a diagonal SBR and opal-based BSR. (a) $T(t)$ function for the synthetic image in figure 13. (b) BSR detection example. The black-dotted lines indicate the SBR and BSR.

A total of 840 synthetic seismic images were used to test the methodology. The system correctly located the BSR and parallel reflectors in synthetic images with non-parallel reflectors and discontinuities (geological faults). Also, the system performed adequately in images with WGN with SNRs of up to 3 dB and with salt-and-pepper noise of up to 0.7 noise density.

3.2. Application to real seismic images

A database of nine seismic images was used to test the proposed methodology. High-resolution 2D multichannel seismic reflection lines were collected in the Farallon Basin in the Gulf of California. Figure 19 shows the area highlighted with a black box, and an amplification of the area is presented in

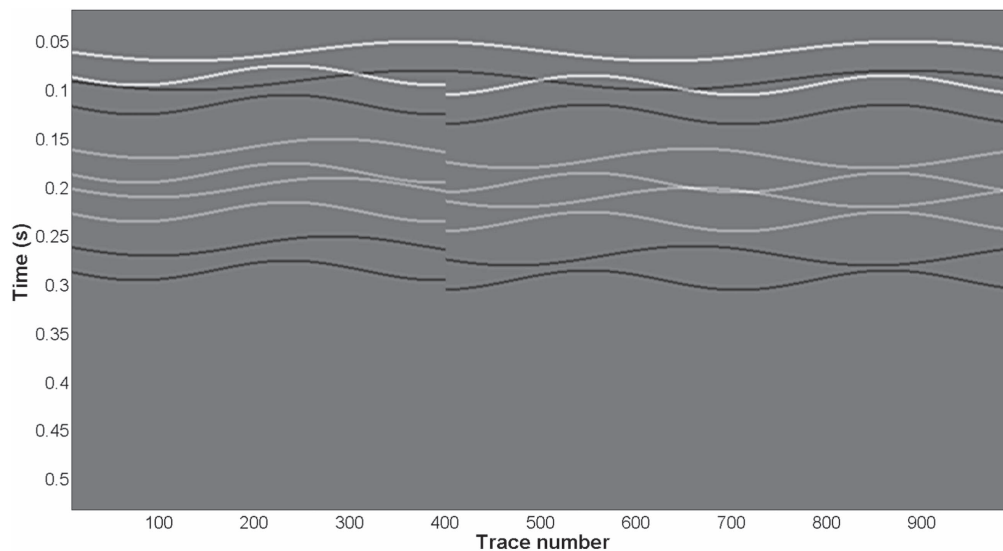


Figure 15. Synthetic seismic image with sinusoidal SBR, gas-based BSR, sinusoidal reflectors non-parallel to SBR and type-two discontinuities.

figure 20, where the seismic profiles are highlighted as black lines. Figure 21 shows a seismic image of geographic coordinates $110^{\circ}\text{W}20'$ latitude and $25^{\circ}\text{N}50'$ longitude in the Farallon Basin. Each seismic image was split into sections of approximately 250 traces (for the real seismic images the distance between traces is 6.25 m); in this manner the computational cost/time of the process is reduced considerably, and, the image could be processed by parallel computing or even handled by a personal computer. An example of the application of the methodology to real data is shown in figures 22 and 23. Figure 22 shows a section of the seismic image from the line located in geographic coordinates $(25.10763^{\circ}, -109.93275^{\circ})$ to $(25.01640^{\circ}, -109.74953^{\circ})$ in the Farallon Basin; its $T(t)$ graph given in figure 23(a) indicates that the BSR appears at $t = 0.035$ s below the SBR and the detected reflectors are highlighted in black-dotted curves in figure 23(b). Figure 24 shows another seismic image where the BSR is not evident and cuts across lithologic reflectors. Figure 25(a) exhibits its $T(t)$ graph indicating that the BSR is located at $t = 0.069$ s below the SBR and it is highlighted in black-dotted curves in figure 25(b). Only parts of the seismic sections present a visible BSR, and some of the sections have other kinds of parallel lines such as multiple and parallel facies. The pattern recognition system locates approximately 95% of the BSRs in the real seismograms.

3.3. Overall performance summary

The 2D multiresolution automated system for detecting the BSR on seismic reflection images detected 100% of the parallel lines in synthetic seismic images with opal- and gas-based BSRs, multiple reflectors parallel to the sea bottom, multiple reflectors non-parallel to the sea bottom and discontinuities (geological faults). In the four scenarios used (each using 15 synthetic seismic images), in the presence of WGN with SNRs of 6 dB to 10 dB, the system successfully detected all parallel lines. For a value of 5 dB it detected 97%

of the parallel reflectors; for 2 dB system efficiency declined to 70% and for 0 dB only 20% were detected (table 1). In the case of salt-and-pepper noise with 0.1 to 0.5 noise density, the system detected 100% of the parallel reflectors; for a value of 0.7 efficiency declined to 93%; and the system obtained 6.7% for a 0.9 noise density (table 2).

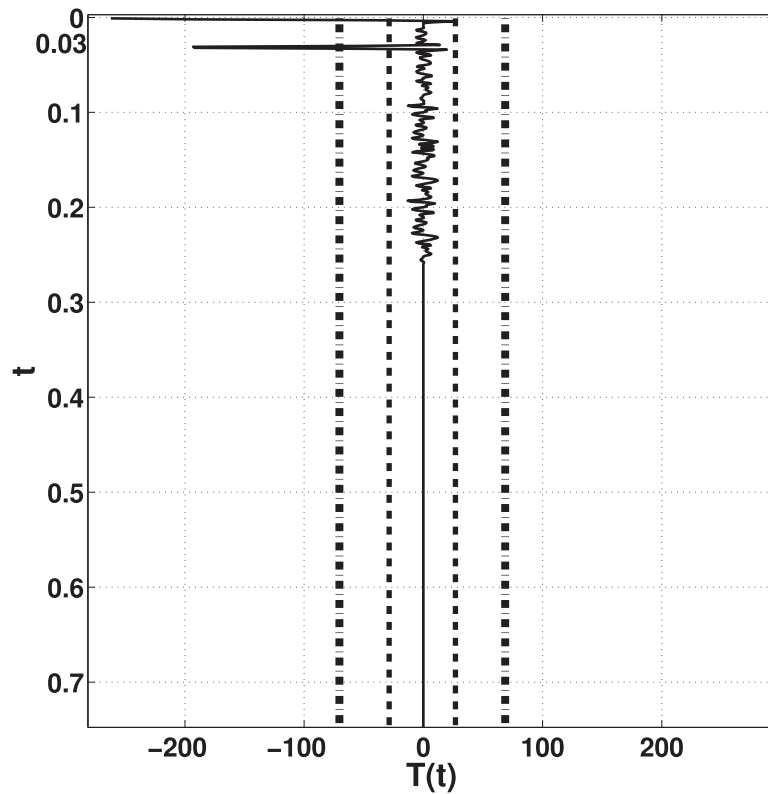
The performance of the pattern recognition system on real data presents an efficiency of 95% on segments that have a BSR or other parallel reflectors to the sea bottom. Moreover, the system detects reflectors that are quasi-parallel depending on their shape and length.

4. Discussion

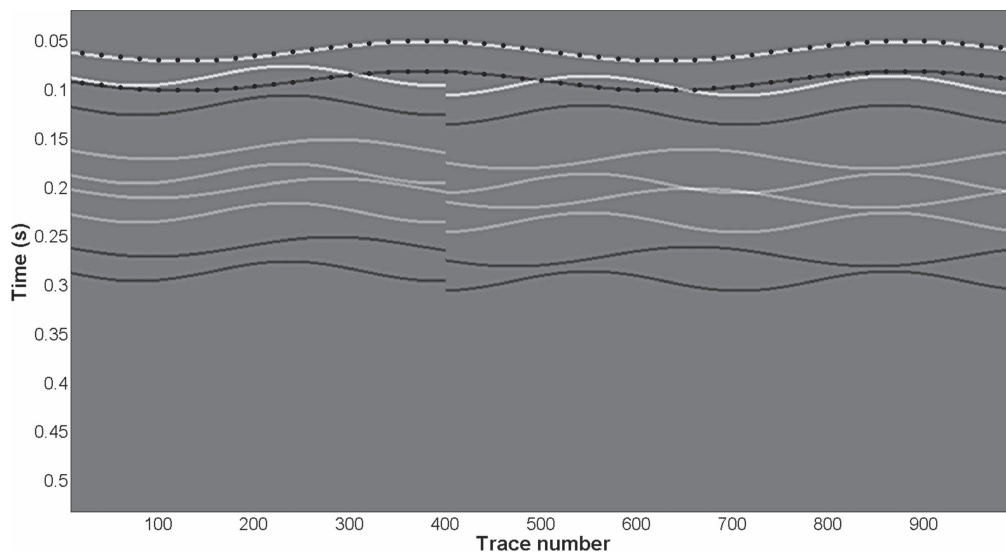
For proper identification of parallel reflectors to the sea bottom, this work takes advantage of 2D MRA. Other approaches, such as comparison through correlation, could cost excessive processing time and are susceptible to noise, yielding unclear results. The Hough transform has been used extensively to detect lines (Duda and Hart 1972), but the use of the Hough transform on noisy images is not efficient, and a denoising step is often necessary. 2D MRA helps by eliminating information on non-horizontal lines and noise; it also enhances the presence of horizontal lines through the use of the HL sub-signal, allowing one to obtain a clear differentiation between reflectors parallel to the sea bottom and other reflectors. This technique could also be applied to multiple elimination processes on seismic reflection images.

5. Conclusions

This paper presents an original methodology that uses 2D MRA to identify the presence of BSRs and other parallel reflectors to the sea bottom. This novel methodology is proved to detect the BSR in synthetic seismic images even in



(a)



(b)

Figure 16. Pattern recognition system response for the synthetic seismic image with non-parallel reflectors and discontinuities (geological faults). (a) $T(t)$ function for the synthetic image in figure 15. (b) Synthetic seismic image with sinusoidal SBR, gas-based BSR, sinusoidal reflectors non-parallel to SBR and type-two discontinuities. The black-dotted curves indicate the detected SBR and BSR.

the presence of high levels of noise and structural situations such as discontinuities (geological faults) and non-parallel reflectors. The methodology has been tested with real seismic reflection images obtained from the Farallon Basin. The images were split into smaller sections considerably reducing computational cost/time; this allows the BSR pattern

recognition methodology to be implemented by parallel computing or handled by personal computers. The methodology shows an efficiency of 95% in the detection of parallel reflectors of the sea bottom even in the presence of non-obvious parallel reflectors or a BSR that cuts across lithologic reflectors.

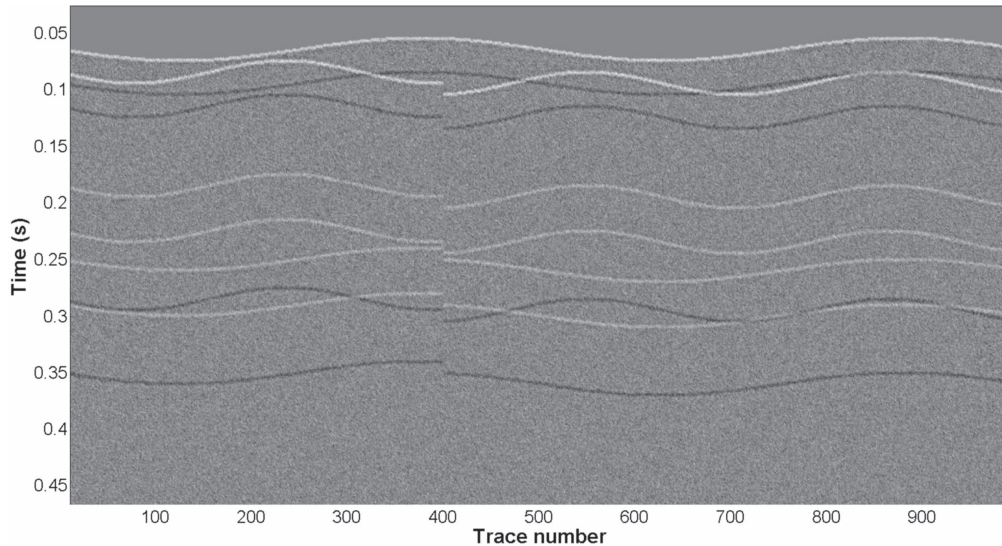


Figure 17. Synthetic seismic image with sinusoidal SBR and gas-based BSR with non-parallel sinusoidal reflectors, type-two discontinuities and WGN with SNR of 6 dB.

Acknowledgments

This work was partially supported by PRODEP and CONACYT under grant number A1-S-33396. Perla Karina Barba Rojo is a student in the PhD program MyDCI offered by UABC and she is supported by a UABC scholarship. The critical grammar review of the manuscript by Andrea Luisa Castro is greatly appreciated.

Appendix A. Wavelet theory

To identify and locate the BSR 2D MRA is used. This methodology uses wavelet subspaces. Therefore the continuous wavelet transform (CWT) and 1D MRA are introduced first. The MRA generalization to 2D is given in appendix B.

A.1. CWT

A family of wavelets can be obtained by translating the b units and scaling the $a \neq 0$ units of the mother wavelet ψ , that is

$$\psi_{a,b}(t) = \frac{1}{\sqrt{|a|}} \psi\left(\frac{t-b}{a}\right), \tag{A.1}$$

for $a, b \in \mathbb{R}$ (Chui 1992).

For a given function $f(t) \in L^2(\mathbb{R})$, Morlet’s CWT is defined as

$$\mathcal{W}(f(t)) = \int_{-\infty}^{\infty} f(t) \overline{\psi_{a,b}(t)} dt, \tag{A.2}$$

where $\overline{\psi_{a,b}(t)}$ is the complex conjugate of $\psi_{a,b}(t)$ and

$$L^2(\mathbb{R}) = \left\{ f : \mathbb{R} \rightarrow \mathbb{C} \mid \int_{-\infty}^{\infty} |f(t)|^2 dt < \infty \right\}. \tag{A.3}$$

The reconstruction of the original function, which is the inverse of the CWT, is given by the double integral

$$f(t) = \frac{1}{C_\psi} \int_{-\infty}^{\infty} \frac{1}{a^2} \int_{-\infty}^{\infty} \mathcal{W}(f(t)) \psi_{a,b}(t) db da, \tag{A.4}$$

where C_ψ is a finite constant defined by the wavelet ψ as

$$C_\psi \equiv \int_{-\infty}^{\infty} \frac{|\mathcal{F}\{\psi(\omega)\}|^2}{|\omega|} d\omega < \infty, \tag{A.5}$$

with \mathcal{F} representing the Fourier transform.

A.2. MRA

The most important feature of MRA is the ability to separate a signal into many components at different scales or resolutions. The idea is to apply a ‘divide and conquer’ strategy to the signal so that individual components may be processed by different algorithms. Hence, two groups of subspaces are introduced to understand the concept of MRA: scaling subspaces and wavelet subspaces.

A scaling function $\varphi(t) \in L^2(\mathbb{R})$ generates a nested sequence of subspaces V_j of L^2 , such that

$$\{0\} \subset \dots \subset V_{-1} \subset V_0 \subset V_1 \subset V_2 \subset \dots \subset L^2. \tag{A.6}$$

Subspace V_j is spanned by

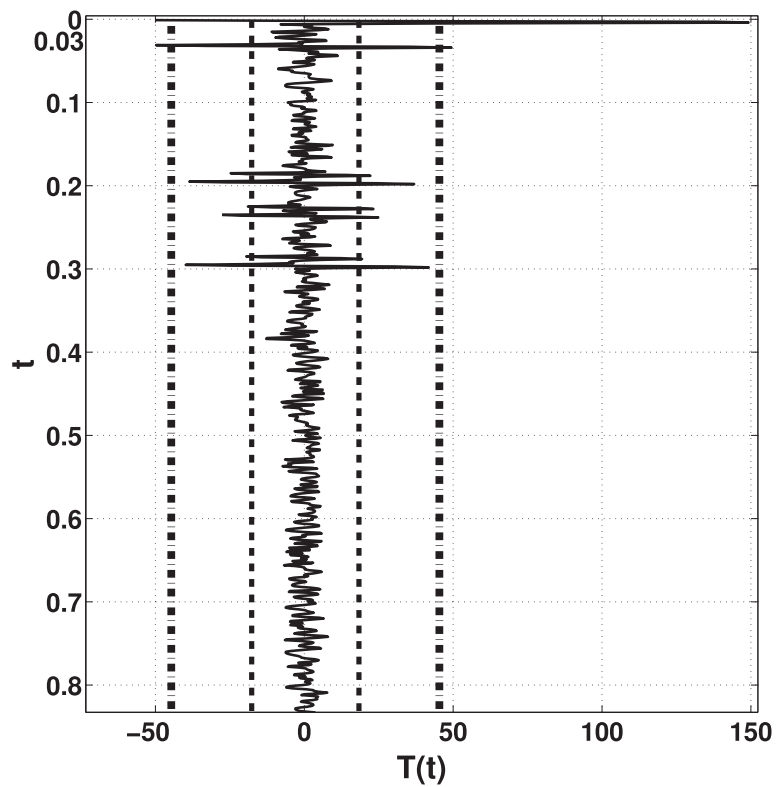
$$\beta_{V_j} = \{ \varphi(2^j t - k) \mid k \in \mathbb{Z} \}; \tag{A.7}$$

therefore the scaling function $\varphi(t)$ could be written as

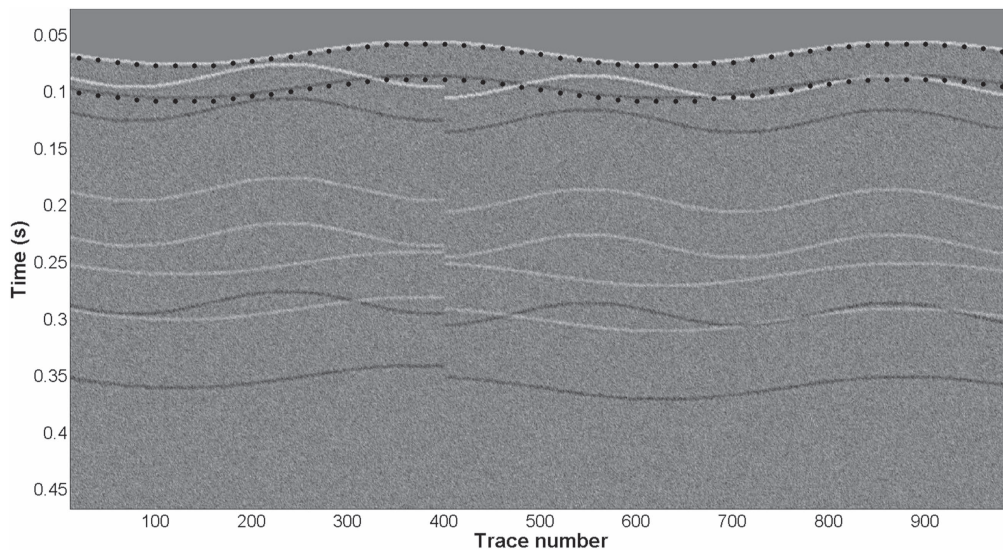
$$\varphi(t) = \sum_{k=-\infty}^{\infty} p_{j,k} \varphi(2^j t - k), \tag{A.8}$$

for $\{p_{j,k}\}_{k=-\infty}^{\infty} \in \ell^2$, where

$$\ell^2 = \left\{ \{ \alpha_k \}_{k=-\infty}^{\infty} \mid \sum_{k=-\infty}^{\infty} |\alpha_k|^2 < \infty \right\}. \tag{A.9}$$



(a)



(b)

Figure 18. Pattern recognition system response for the synthetic seismic image with WGN with SNR of 6 dB. (a) $T(t)$ function for the synthetic image in figure 17. (b) Synthetic seismic image with sinusoidal SBR and gas-based BSR with non-parallel sinusoidal reflectors, type-two discontinuities and WGN with SNR of 6 dB. The black-dotted curves indicate the detected SBR and BSR.

Table 1. The efficiency of the pattern recognition system response on synthetic seismic images in the presence of different levels of WGN.

SNR			Scenario			
dB	%	variance	Sea bottom and parallel reflectors	Sea bottom, parallel and non-parallel reflectors	Sea bottom, parallel and non-parallel reflectors and type-one discontinuities	Sea bottom, parallel and non-parallel reflectors and type-two discontinuities
10	1000	0.1	100%	100%	100%	100%
8	631	0.15	100%	100%	100%	100%
6	398	0.25	100%	100%	100%	100%
5	316.50	0.32	97%	97%	97%	97%
3	200	0.51	97%	97%	97%	97%
2	158.50	0.63	70%	70%	70%	70%
1	125.80	0.80	37%	37%	37%	37%
0	100	1.00	20%	20%	20%	20%

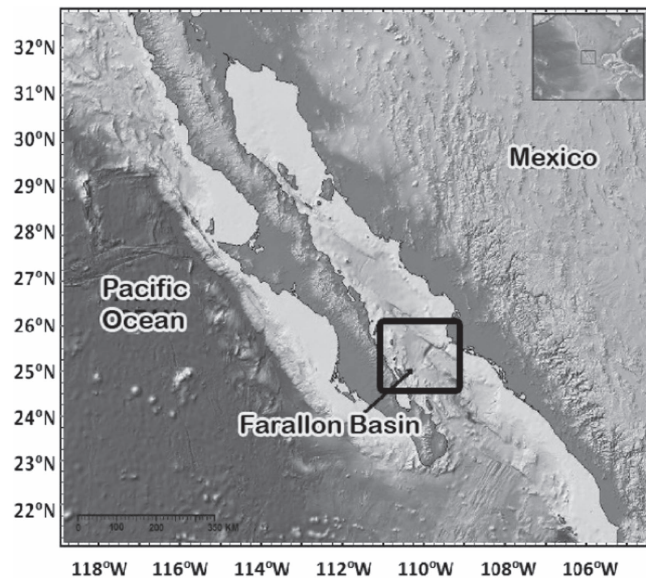


Figure 19. Bathymetric map and digital elevation model of northwestern Mexico. The study area in the Farallon Basin at the Gulf of California is highlighted with a black box. Reproduced with permission from (2011).

To simplify the notation: $\varphi(2^j - k) \equiv \varphi_{j,k}(t)$. Wavelet space W_j is defined as

$$V_{j+1} = V_j \oplus W_j, \tag{A.10}$$

that is, W_j is the orthogonal complement of V_j in subspace V_{j+1} . Subspace W_j is spanned by

$$\beta_{w_j} = \{\psi(2^j t - k) | k \in \mathbb{Z}\}; \tag{A.11}$$

hence

$$\psi(t) = \sum_{k=-\infty}^{\infty} q_{j,k} \psi(2^j t - k), \tag{A.12}$$

for $\{q_{j,k}\}_{k=-\infty}^{\infty} \in \ell^2$. To simplify the notation: $\psi(2^j - k) \equiv \psi_{j,k}(t)$. Since

$$\varphi(t) \in V_j \subset V_{j+1}, \tag{A.13}$$

$$\psi(t) \in W_j \subset V_{j+1}, \tag{A.14}$$

these equations (A.13, A.14) provide the relations of a function between two different scales

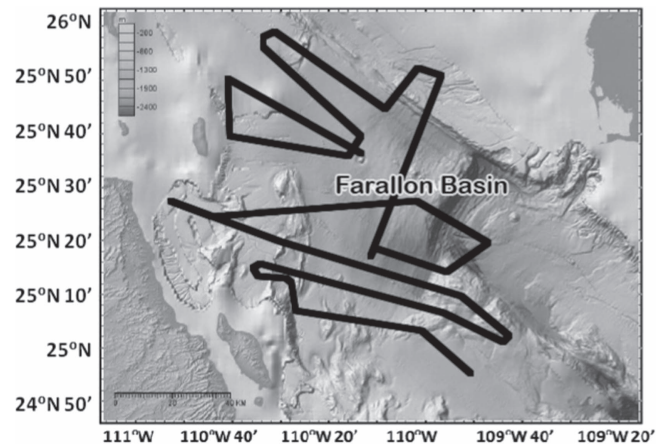


Figure 20. Amplification of the study area in the Farallon Basin. Seismic profiles highlighted with black lines. Reproduced with permission from (2011).

$$\varphi(2^j t) = \sum_{k=-\infty}^{\infty} p_{j+1,k} \varphi(2^{j+1} t - k), \tag{A.15}$$

$$\psi(2^j t) = \sum_{k=-\infty}^{\infty} q_{j+1,k} \varphi(2^{j+1} t - k), \tag{A.16}$$

which are often referred to as the reconstruction (synthesis) relations. The decomposition (analysis) relation is used to separate the signal into different scales or resolutions. In order to establish this, let us use equation (A.10) to write $\varphi_{j+1,l}(t) \in V_{j+1}$ in terms of the linear combination of elements in V_j and W_j :

$$\varphi_{j+1,l}(t) = \varphi(2^{j+1} t - l) = \sum_{k=-\infty}^{\infty} \{a_{j,k}^{(l)} \varphi_{j,k}(t) + b_{j,k}^{(l)} \psi_{j,k}(t)\}, \tag{A.17}$$

where $l \in \mathbb{Z}$ and $\{a_{j,k}^{(l)}\}_{k=-\infty}^{\infty}, \{b_{j,k}^{(l)}\}_{k=-\infty}^{\infty} \in \ell^2$.

For $f_{j+1} \in V_{j+1}, f_j \in V_j$ and $g_j \in W_j$,

$$f_{j+1}(t) = \sum_{l=-\infty}^{\infty} c_{j+1,l} \varphi_{j+1,l}(t), \tag{A.18}$$

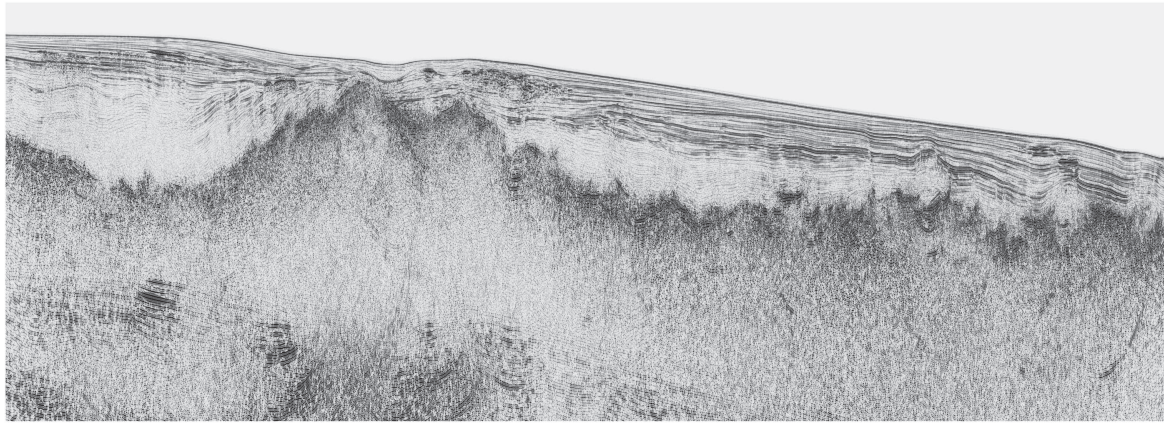


Figure 21. Seismic image of the line located in geographic coordinates (25.985 62°, -110.521 02°) to (25.943 03°, -110.568 07°) in the Farallon Basin.

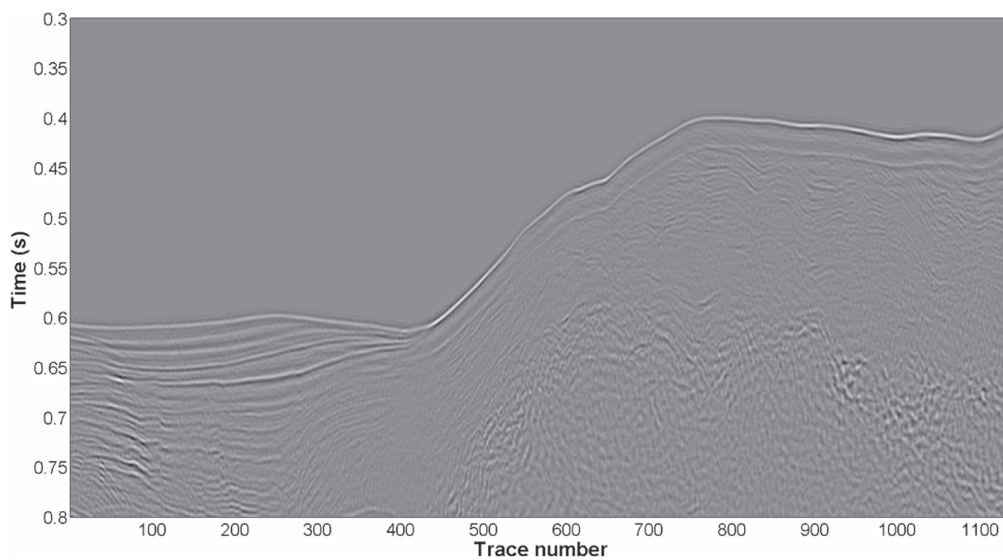


Figure 22. Section of the seismic image of the line located in geographic coordinates (25.107 63°, -109.932 75°) to (25.016 40°, -109.749 53°) in the Farallon Basin.

Table 2. The efficiency of the pattern recognition system response on synthetic seismic images in the presence of different levels of salt-and-pepper noise.

Density	Scenario			
	Sea bottom and parallel reflectors	Sea bottom, parallel and non-parallel reflectors	Sea bottom, parallel and non-parallel reflectors and type-one discontinuities	Sea bottom, parallel and non-parallel reflectors and type-two discontinuities
0.1	100%	100%	100%	100%
0.3	100%	100%	100%	100%
0.5	100%	100%	100%	100%
0.7	93%	93%	93%	93%
0.8	57%	57%	57%	57%
0.9	6.70%	6.70%	6.70%	6.70%

$$f_j(t) = \sum_{k=-\infty}^{\infty} c_{j,k} \varphi_{j,k}(t), \tag{A.19}$$

$$g_j(t) = \sum_{k=-\infty}^{\infty} d_{j,k} \psi_{j,k}(t), \tag{A.20}$$

and because $V_{j+1} = V_j \oplus W_j$, it is possible to state that

$$f_{j+1}(t) = f_j(t) + g_j(t). \tag{A.21}$$

Substituting relations (A.18), (A.19) and (A.20) in equation (A.21) yields

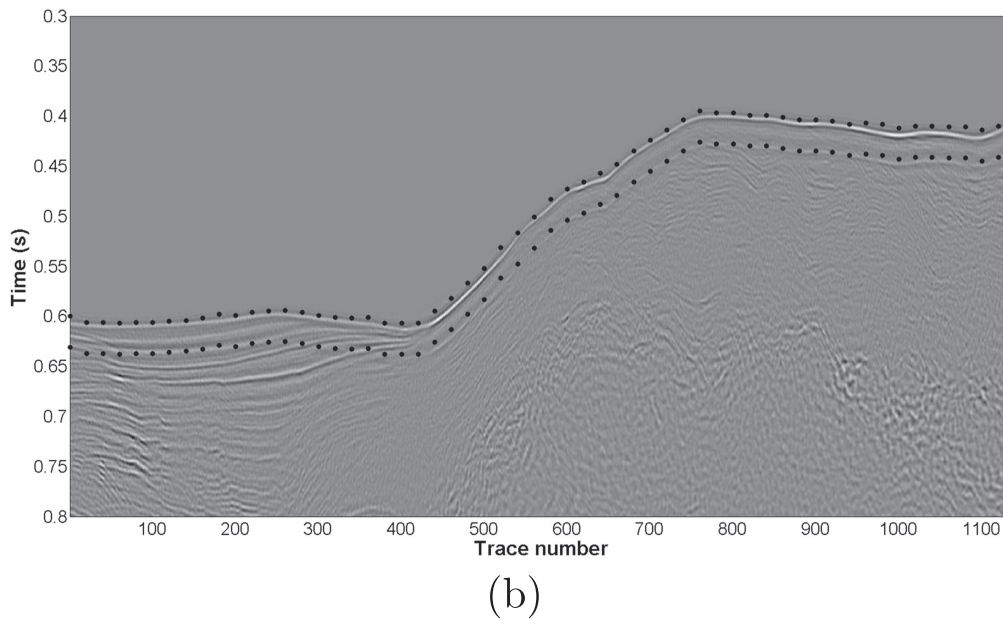
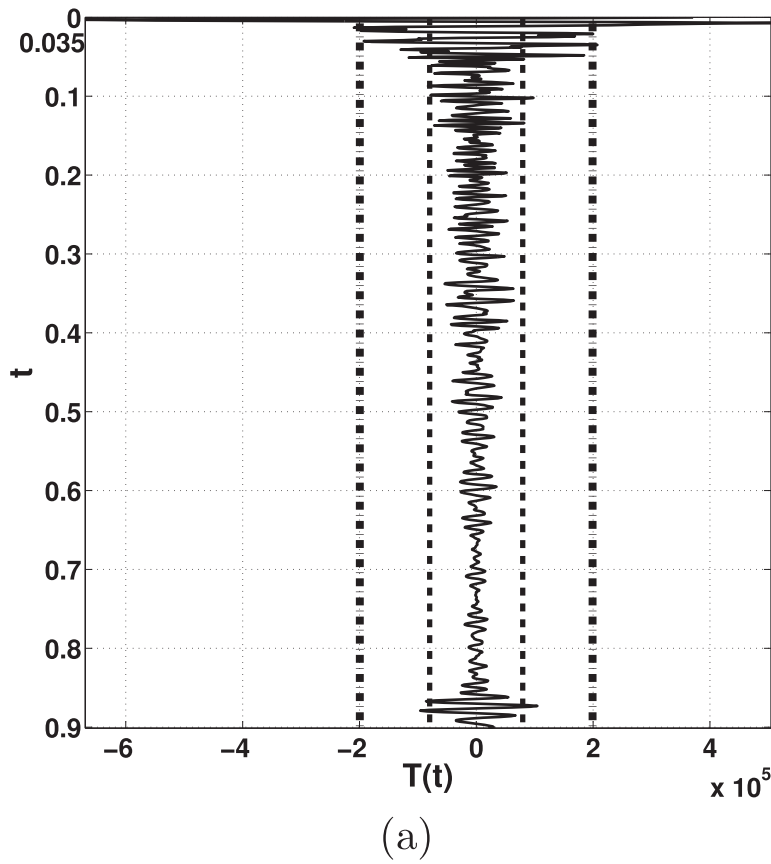


Figure 23. Pattern recognition system response for a real seismic image from the Farallon Basin. (a) $T(t)$ function for the image in figure 22. (b) BSR detection example for the image in figure 22. The black-dotted curves indicate the SBR and BSR.

$$\sum_{l=-\infty}^{\infty} c_{j+1,l} \varphi_{j+1,l}(t) = \sum_{k=-\infty}^{\infty} c_{j,k} \varphi_{j,k}(t) + \sum_{k=-\infty}^{\infty} d_{j,k} \psi_{j,k}(t). \tag{A.22}$$

$$\sum_{k=-\infty}^{\infty} \left\{ \sum_{l=-\infty}^{\infty} [a_{j,k}^{(l)} c_{j+1,l} \phi_{j,k}(t)] + \sum_{k=-\infty}^{\infty} [b_{j,k}^{(l)} c_{j+1,l} \psi_{j,k}(t)] \right\} = \sum_{k=-\infty}^{\infty} [c_{j,k} \phi_{j,k}(t) + d_{j,k} \psi_{j,k}(t)]. \tag{A.23}$$

Using equation (A.17) on the left-hand side of equation (A.22) yields

By the polynomial equality property,

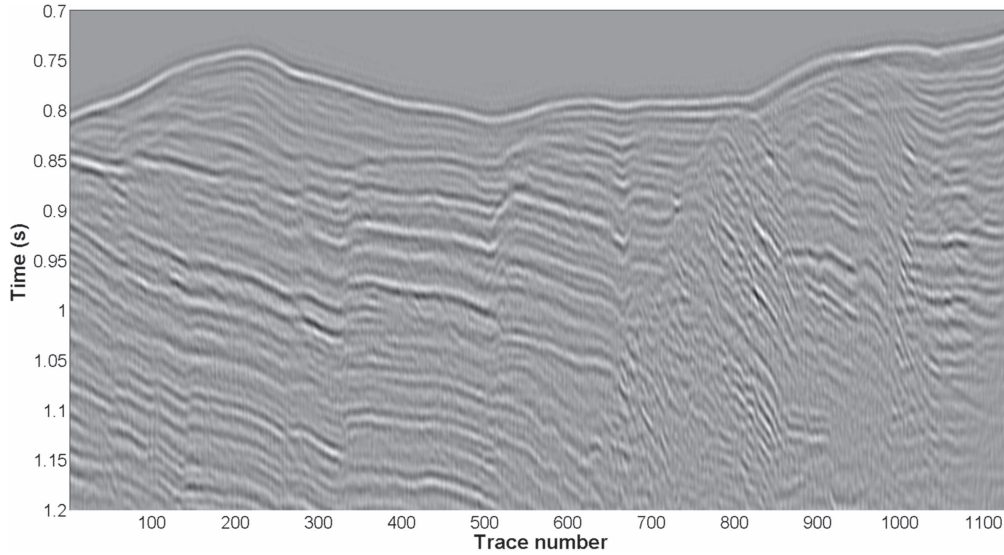


Figure 24. Section of the seismic image of the line located in geographic coordinates (25.457 98°, -110.038 68°) to (25.341 15°, -109.790 95°) in the Farallon Basin.

$$c_{j,k} = \sum_{l=-\infty}^{\infty} a_{j,k}^{(l)} c_{j+1,l}, \quad (\text{A.24})$$

$$d_{j,k} = \sum_{l=-\infty}^{\infty} b_{j,k}^{(l)} c_{j+1,l}; \quad (\text{A.25})$$

this is equal to passing the signal through a pair of analysis filters that comprises a low-pass filter $a_{j,k}^{(l)}$ and a high-pass filter $b_{j,k}^{(l)}$. After that, down-sampling by a factor of 2 is applied to each sub-signal, as illustrated in figure A1.

The synthesis equation is obtained using the relations given in A.15 and A.16 on the right-hand side of equation (A.22), yielding

$$\begin{aligned} & \sum_{l=-\infty}^{\infty} c_{j+1,l} \varphi_{j+1,l}(t) \\ &= \sum_{l=-\infty}^{\infty} \sum_{k=-\infty}^{\infty} [c_{j,k} p_{j+1,l}^{(k)} + d_{j,k} q_{j+1,l}^{(k)}] \varphi_{j+1,l}(t); \end{aligned} \quad (\text{A.26})$$

by the polynomial equality property,

$$c_{j+1,l} = \sum_{k=-\infty}^{\infty} [c_{j,k} p_{j+1,l}^{(k)} + d_{j,k} q_{j+1,l}^{(k)}], \quad (\text{A.27})$$

which corresponds to up-sampling before convolution, as illustrated in figure A1 (Furati and Siddiqi 2005).

Appendix B. 2D MRA

In order to extend the MRA, explained in appendix A.2, to 2D signals (Chui 1992), a scaling space V_j^2 is constructed by

$$V_j^2 = V_j \otimes V_j, \quad (\text{B.1})$$

the scaling function Φ is described by

$$\Phi(x, y) = \varphi(x) \varphi(y), \quad (\text{B.2})$$

and subspace V_j^2 is spanned by

$$\beta_{V_j^2} = \{\Phi_{j,k,m}(x, y) | k, m \in \mathbb{Z}\}, \quad (\text{B.3})$$

where

$$\Phi_{j,k,m}(x, y) = \varphi_{j,k}(x) \varphi_{j,m}(y). \quad (\text{B.4})$$

Wavelet space W_j^2 is the orthogonal complement of V_j^2 , given by

$$V_{j+1}^2 = V_j^2 \oplus W_j^2, \quad (\text{B.5})$$

for $j \in \mathbb{Z}$. Mallat (1989) established that W_j^2 has an orthonormal basis

$$\beta_{W_j^2} = \{\Psi_{j,k,m}^{(1)}, \Psi_{j,k,m}^{(2)}, \Psi_{j,k,m}^{(3)} | k, m \in \mathbb{Z}\}, \quad (\text{B.6})$$

where

$$\Psi_{j,k,m}^{(1)}(x, y) = \varphi_{j,m}(x) \psi_{j,m}(y), \quad (\text{B.7})$$

$$\Psi_{j,k,m}^{(2)}(x, y) = \psi_{j,m}(x) \varphi_{j,m}(y), \quad (\text{B.8})$$

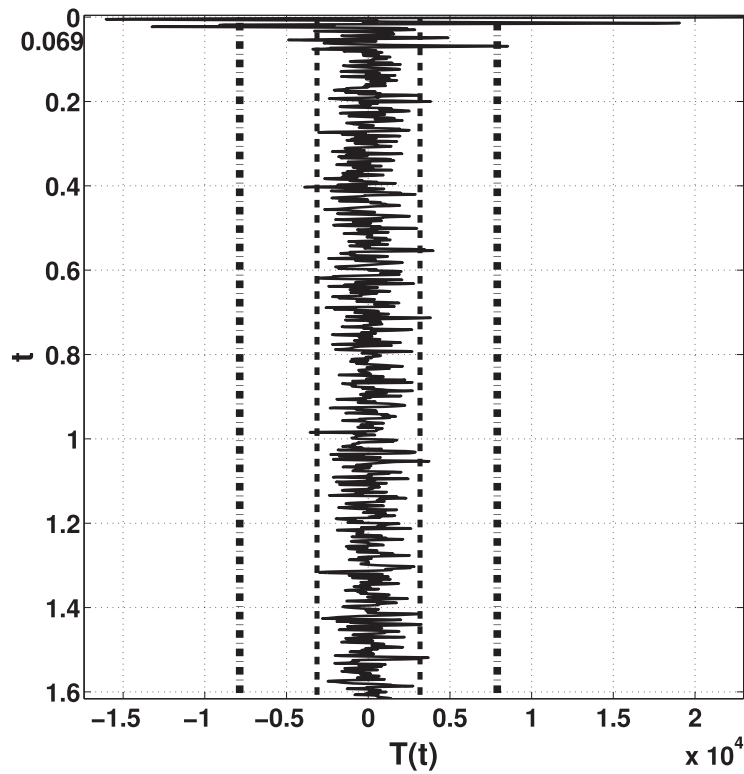
$$\Psi_{j,k,m}^{(3)}(x, y) = \psi_{j,m}(x) \psi_{j,m}(y). \quad (\text{B.9})$$

Substituting A.10 in B.1 yields

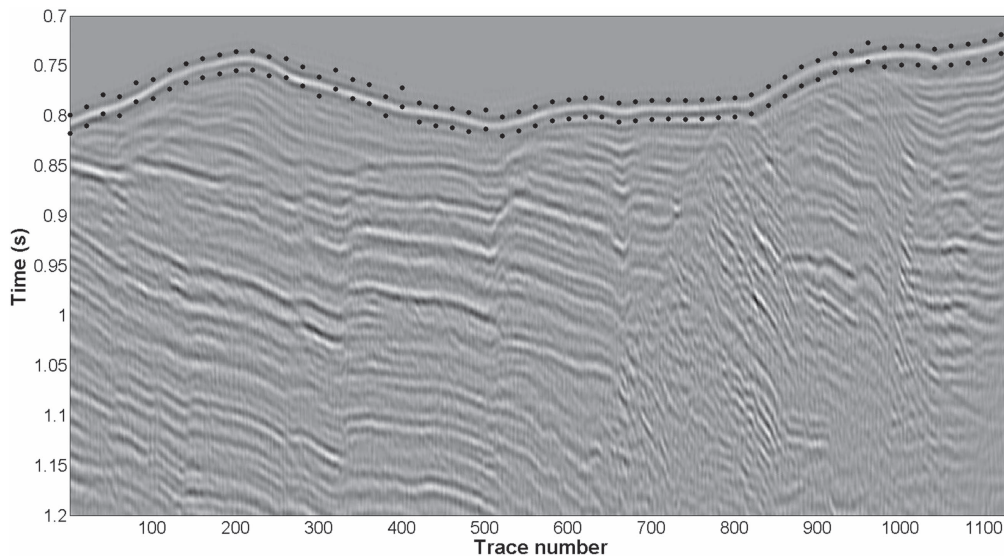
$$\begin{aligned} V_{j+1}^2 &= V_{j+1} \otimes V_{j+1} = (V_j \oplus W_j) \otimes (V_j \oplus W_j) = (V_j \otimes V_j) \\ &\quad \oplus (V_j \otimes W_j) \oplus (W_j \otimes V_j) \oplus (W_j \otimes W_j) \\ &= (V_j \otimes V_j) \oplus \underbrace{[(V_j \otimes W_j) \oplus (W_j \otimes V_j) \oplus (W_j \otimes W_j)]}_{W_j^2}, \end{aligned} \quad (\text{B.10})$$

that is, equation (B.10) splits the 2D signal into four different sub-signals (Chui 1992):

- LL sub-signal: This contains the horizontal and vertical low frequencies of the signal. The sub-signal belongs to subspace $V_j \otimes V_j$, which is spanned by $\{\Phi_{j,k,m}(x, y) | k, m \in \mathbb{Z}\}$.
- LH sub-signal: This contains the horizontal low frequencies and vertical high frequencies of the signal. The sub-



(a)



(b)

Figure 25. Pattern recognition system response for a real seismic image from Farallon Basin. (a) $T(t)$ function for the image in figure 24. (b) BSR detection example for the image in figure 24. The black-dotted curves indicate the SBR and BSR.

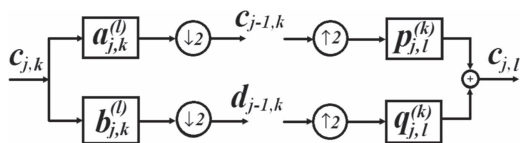


Figure A1. Block diagram of the analysis-and-synthesis methodology.

signal belongs to subspace $V_j \otimes W_j$, which is spanned by $\{\Psi_{j,k,m}^{(1)}(x, y) | k, m \in \mathbb{Z}\}$.

- HL sub-signal: This contains the vertical low frequencies and horizontal high frequencies of the signal. The sub-signal belongs to subspace $W_j \otimes V_j$, which is spanned by $\{\Psi_{j,k,m}^{(2)}(x, y) | k, m \in \mathbb{Z}\}$.

- HH sub-signal: This contains the horizontal and vertical high frequencies of the signal. The sub-signal belongs to subspace $W_j \otimes W_j$, which is spanned by $\{\Psi_{j,k,m}^{(3)}(x, y) | k, m \in \mathbb{Z}\}$.

ORCID iDs

Selene Solorza-Calderón  <https://orcid.org/0000-0002-7935-6063>

Antonio González-Fernández  <https://orcid.org/0000-0002-0910-8240>

Mario González-Escobar  <https://orcid.org/0000-0002-6061-9695>

References

- Akram J and Eaton D 2016 A review and appraisal of arrival-time picking methods for downhole microseismic data *Geophysics* **81** KS71–KS91
- Aregbe A 2017 Gas hydrate-properties, formation and benefits *Open J. Yangtze Gas Oil* **2** 27–44
- Berndt C, Bünz S, Clayton T, Mienert J and Saunders M 2004 Seismic character of bottom simulating reflectors: examples from the mid-Norwegian margin *Mar. Pet. Geol.* **21** 723–33
- Boswell R and Collett T 2011 Current perspectives on gas hydrate resources *Energy Environ. Sci.* **4** 1206–15
- Bünz S and Mienert J 2004 Acoustic imaging of gas hydrate and free gas at the Storegga Slide *J. Geophys. Res.* **109** B04102
- Carcione J and Tinivella U 2000 Bottom-simulating reflectors: seismic velocities and AVO effects *Geophysics* **65** 54–67
- Castellazzi C, Savage M, Walsh E and Arnold R 2015 Shear wave automatic picking and splitting measurements at Ruapehu volcano, New Zealand *J. Geophys. Res.: Solid Earth* **120** 3363–84
- Chui C 1992 *An Introduction to Wavelets* (San Diego, CA: Academic)
- Coren F, Volpi V and Tinivella U 2001 Gas hydrate physical properties imaging by multi-attribute analysis -Blake Ridge BSR case history *Mar. Geol.* **178** 197–210
- Deep R 2006 *Probability and Statistics* (San Diego, CA: Elsevier/Academic)
- Dobrin M and Savit C 1988 *Introduction to Geophysical Prospecting* (New York: McGraw-Hill)
- Duda R and Hart P 1972 Use of the Hough transformation to detect lines and curves in pictures *Commun. ACM* **15** 11–5
- Furati K and Siddiqi A 2005 *Mathematical Models and Methods for Real World Systems, Lecture Notes in Pure and Applied Mathematics* (Boca Raton, FL: Chapman & Hall/CRC Press)
- Gentili S and Michelini A 2006 Automatic picking of P and S phases using a neural tree *J. Seismol.* **10** 39–63
- Gonzalez R and Woods R 2008 *Digital Image Processing (3rd edn)* (Upper Saddle River, NJ: Pearson/Prentice Hall)
- Holbrook W, Hoskins H, Wood W, Stephen R and Lizarralde D 1996 Methane hydrate and free gas on the Blake Ridge from vertical seismic profiling *Science* **273** 1840–3
- Klitzke P, Luzi-Helbing M, Schicks J, Cacace M, Jacquy A, Sippel J, Scheck-Wenderoth M and Faleide J 2016 Gas hydrate stability zone of the Barents Sea and Kara Sea region *Energy Procedia* **97** 302–9
- Koh C and Sloan E 2007 Natural gas hydrates: recent advances and challenges in energy and environmental applications *Am. Inst. Chem. Eng.* **53** 1636–43
- MacKay M, Jarrard R, Westbrook G and Hyndman R 1994 Origin of bottom-simulating reflectors: geophysical evidence from the Cascadia accretionary prism *Geology* **22** 459–62
- Maity D, Aminzadeh F and Karrenbach M 2014 Novel hybrid artificial neural network based autopicking workflow for passive seismic data *Geophys. Prospect.* **62** 834–47
- Majorowicz J and Osadetz K 2003 Natural gas hydrate stability in the East Coast offshore-Canada *Nat. Resour. Res.* **12** 93–104
- Mallat S 1989 A theory for multiresolution signal decomposition: the wavelet representation *IEEE Trans. Pattern Anal. Mach. Intell.* **11** 674–93
- McCormack M, Zaucha D and Dushek D 1993 First-break refraction event picking and seismic data trace editing using neural networks *Geophysics* **58** 67–78
- Nouzè H, Cosquer E, Collot J, Foucher J, Klingelhoefer F, Lafoy Y and Gèli L 2009 Geophysical characterization of bottom simulating reflectors in the Fairway Basin (off New Caledonia, Southwest Pacific), based on high resolution seismic profiles and heat flow data *Mar. Geol.* **266** 80–90
- Oellrich L 2004 Natural gas hydrates and their potential for future energy supply 'XVII National and VI ISHMT/ASME Heat and Mass Transfer Conf.' Vol. K9 of IGCAR (Washington, DC: American Society of Mechanical Engineers) pp 70–8
- IPCC 2014 *Climate Change 2014: Synthesis Report. Contribution of Working Groups I, II and III to the Fifth Assessment Report of the Intergovernmental Panel on Climate Change* (Geneva: IPCC)
- Pecher I, Minshull T, Singh S and von Huene R 1996 Velocity structure of a bottom simulating reflector offshore Peru: results from full waveform inversion *Earth Planet. Sci. Lett.* **139** 459–69
- Plaza-Faverola A, Vadakkepuliambatta S, Hong W, Mienert J, Bünz S, Chand S and Greinert J 2017 Bottom-simulating reflector dynamics at Arctic thermogenic gas provinces: an example from Vestnesa Ridge, offshore west Svalbard *J. Geophys. Res.: Solid Earth* **122** 4089–105
- Rodrigo C, González-Fernández A and Vera E 2009 Variability of the bottom-simulating reflector (BSR) and its association with tectonic structures in the Chilean margin between Arauco Gulf (37°S) and Valdivia (40°S) *Mar. Geophys. Res.* **30** 1–19
- Rodrigo C, Vera E and González-Fernández A 2009 Seismic analysis and distribution of a bottom-simulating reflector (BSR) in the Chilean margin offshore of Valdivia (40° S) *J. South Am. Earth Sci.* **27** 1–10
- Ruppel C and Kessler J 2017 The interaction of climate change and methane hydrates *Rev. Geophys.* **55** 126–68
- Sandham W and Leggett M 2003 *Geophysical Applications of Artificial Neural Networks and Fuzzy Logic (Modern Approaches in Geophysics vol 21)* (Dordrecht: Springer Science+Business Media)
- Taladay K, Boston B and Moore G 2017 Gas-in-place estimate for potential gas hydrate concentrated zone in the Kumano Basin, Nankai Trough Forearc, Japan *Energies* **10** 1552
- Tang Y, Ma H, Liu J, Li B F and Xi D 1997 Multiresolution analysis in extraction of reference lines from documents with gray level background *IEEE Trans. Pattern Anal. Mach. Intell.* **19** 921–6
- Teutle A 2011 Evidencias de gas en sedimentos de la Cuenca Farallón, Golfo de California, a partir de las características de sísmica de reflexión *MSc Thesis Ciencias de la Tierra, CICESE, Mexico*
- Tinivella U 1999 A method for estimating gas hydrate and free gas concentrations in marine sediments *Boll. Geofis. Teor. Appl.* **40** 19–30
- Tinivella U and Carcione J 2001 Estimation of gas-hydrate concentration and free-gas saturation from log and seismic data *Leading Edge* **20** 200–3

- Triola M 2010 *Elementary Statistics* 11th edn (Boston, MA: Addison-Wesley)
- Vadakkepuliyambatta S, Skeie R, Myhre G, Dalsoren S, Silyakova A, Schmidbauer N, Myhre C and Mienert J 2017 Climatic impact of Arctic Ocean methane hydrate dissociation in the 21st-century *Earth Syst. Dyn.* **1–27**
- Vargas-Cordero I, Tinivella U and Villar-Muñoz L 2017 Gas hydrate and free gas concentrations in two sites inside the Chilean margin (Itata and Valdivia offshores) *Energies* **10** **2154**
- Yuan S, Liu J, Wang S, Wang T and Shi P 2018 Seismic waveform classification and first-break picking using convolutional neural networks *IEEE Geosci. Remote Sens. Lett.* **15** **272–6**